Journal of Nuclear Medicine, published on December 5, 2019 as doi:10.2967/jnumed.119.233155

Title: Label-free Visualization of Early Cancer Hepatic Micrometastasis and Intraoperative Image-guided Surgery by Photoacoustic Imaging

Running title: Hepatic micrometastasis early detection

Qian Yu[1,#], Shanshan Huang[1,#], Zhiyou Wu[1], Jiadi Zheng[2], Xiaoyuan Chen[3], and Liming Nie[1,*]

[1]State Key Laboratory of Molecular Vaccinology and Molecular Diagnosis & Center for Molecular Imaging and Translational Medicine, School of Public Health, Xiamen University, Xiamen 361102, China.

[2]Department of Neurosurgery, Xiamen hospital of Beijing University Traditional Chinese Medicine, Xiamen 361001, China.

[3]Laboratory of Molecular Imaging and Nanomedicine, National Institute of Biomedical Imaging and Bioengineering, National Institutes of Health, Bethesda, Maryland 20892, USA

[#]**First authors:** These authors contributed equally to this work. State Key Laboratory of Molecular Vaccinology and Molecular Diagnosis & Center for Molecular Imaging and Translational Medicine, School of Public Health, Xiamen University, Xiang'an South Road, Xiang'an district, Xiamen 361102, P. R. China.

***Corresponding author:**

Liming Nie, State Key Laboratory of Molecular Vaccinology and Molecular Diagnosis & Center for Molecular Imaging and Translational Medicine, School of Public Health, Xiamen University, Xiang'an South Road, Xiang'an district, Xiamen 361102, P. R. China. E-mail address: nielm@xmu.edu.cn. Phone & Fax: +86-0592-2880642

ABSTRACT

Objectives: The detection of cancer micrometastasis for early diagnosis and treatment poses a great challenge for conventional imaging techniques. The aim of study is to evaluate the performance of photoacoustic imaging (PAI) in detecting hepatic micrometastases from melanoma in a very early stage and perform tumor resection by intraoperative photoacoustic image-guidance.

Methods: In vivo studies were performed by following protocols approved by the Ethical Committee for Animal Research at Xiamen University. First, a B16 melanoma hepatic metastasis mouse model (n = 10) was established to study the development of micrometastases in vivo. Next, the hepatic metastasis mice models were imaged by scalable PAI instrument, ultrasound, 9.4 T high-resolution magnetic resonance imaging (MRI), positron emission tomography/computed tomography (PET/CT), and bioluminescence imaging. Photoacoustic images acquired with optical wavelengths spanning from 680 to 850 nm were spectrally unmixed by using a linear least-squares method to differentiate various components. Differences in the signal-to-background ratios among different modalities were determined with the two-tailed paired t test. The diagnosis results were assessed with histologic examinations. Excised liver samples from patients diagnosed with hepatic cancer were also examined to identify tumor boundary. In viv*o* metastatic melanoma removal in surgery was precisely guided by the portable PAI system.

Results: PAI achieved as small as ~400 μm hepatic melanoma detection at a depth up to 7 mm in vivo, which could early detect small melanoma compared with ultrasound and MRI in mouse models. The signal ratio of tumor-to-liver acquired with PAI in micrometastases at 8 days (4.2 ± 0.2, n = 6) and 14 days (9.2 ± 0.4, n = 5) were significantly higher than those obtained with PET/CT (1.8 ± 0.1, n = 5 and 4.5 ± 0.2, n = 5, P <0.001 for both). Functional PAI provided dynamic oxygen saturation changes during tumor growth. The limit of detection was measured to be approximately 219 cells per microliter in vitro. We

successfully performed intraoperative photoacoustic image-guided surgery in vivo using the rapid portable PAI system.

Conclusions: Our findings offer a rapid and effective tool to noninvasively detect micrometastases and guide intraoperative resection as a complementary clinical imaging application.

Keywords: Micrometastasis, Visualization, Early stage, Intraoperative navigation, Photoacoustic imaging

INTRODUCTION

Melanoma is a malignant tumor of the skin and has shown a steady increase in its incidence in the past few decades (*1*). Melanoma metastasis consists of a consecutive series of steps, including exfoliation from primary tumors, the survival of tumor cells in circulation, staying in new organs, exudation to surrounding tissues and angiogenesis of metastatic tumors, which ultimately proliferate in a new environment (*2,3*). Malignant melanoma cells shed from the primary tumor often metastasize to the lymph nodes (*4*), liver (*5*), lungs (*6*), and brain (*7*). The liver is the most frequently involved organ by metastatic choroidal melanoma (*8*). The cutaneous melanoma metastasizes to liver less frequently but 15-20% of metastatic melanoma still occur in liver (*9*). The survival rate of melanoma hepatic metastasis patients has been reported to be low (*10*). Due to its aggressive progression and high metastasis risk, it is associated with poor prognosis, as well as high morbidity and mortality rates (*11*). Therefore, accurate diagnosis of hepatic melanoma micrometastasis at the early stage is critical to improve the prognosis and survival rate of the patients.

Metastasis in clinic is usually detected by imaging methods including ultrasound, magnetic resonance imaging (MRI), and positron emission tomography/computed tomography (PET/CT). While ultrasound imaging lacks sufficient contrast in soft tissue and cannot detect blood oxygenation, MRI is not the primary choice for the liver due to its suboptimal sensitivity, long scanning time, and high operational costs. PET is useful for detecting cancer metastasis and monitoring therapeutic response, but the 2-deoxy-2-^{18}F fluorodeoxyglucose (^{18}F-FDG) may yield false-positive results in patients with other symptoms along with high examination fee (*12*). Therefore, the current clinical imaging modalities are not ideal for detecting small tumors and micrometastasis.

Photoacoustic imaging (PAI) is a noninvasive method that combines high spatial resolution of ultrasound with rich contrast of optical imaging (*13*). It allows high-precision imaging and characterization of molecules, cells, tissues, and organs (*14*), so that feature

extraction can be acquired from photoacoustic images (*15*). PAI can provide endogenous contrast among different anatomical structures on account of intrinsic light absorbers *e.g.* hemoglobin (*16*), lipid (*17*), and melanin (*18*). Ex vivo PAI of melanin in the resected sentinel lymph nodes shows excellent correlation with histological melanoma cell infiltration (*19*). In addition, in vivo PAI can track unmarked circulating melanoma cells, image functional connections between blood vessels and whole brains (*20*), and quantify blood flow and oxygen metabolism of the lesions (*21*). It combines advantages of high resolution, high sensitivity, and deep penetration, enabling early diagnosis of hepatic micrometastasis.

A high recurrence rate after tumor resection is due to the incomplete removal of the malignant mass, which results in residual cancer cells. The surgeons primarily rely on visual and tactile identification of the cancerous tissue in order to distinguish it from the benign tissue, which is often inaccurate. PAI possesses optimal resolution and imaging depth in the liver, which is far superior to the limited resolution and imaging depth of fluorescence imaging (*22*). As a label-free technique, PAI obviates the shortcomings of widely used fluorescence imaging which requires gene expression or injection of fluorescence probes (*23,24*). PAI offers excellent spatial and temporal resolution to accurately determine the tumor margin and tissue structure (*25*), and is therefore a viable option for early-stage cancer detection. In addition, its portable setup and hand-held probe save time and labor.

Resection is the basic method of treatment for liver metastatic tumors, and it offers the optimal long-term survival rate. Previous study has combined MRI, PAI and Raman imaging to guide intraoperative tumor resection by intravenous injection of nanoparticles (*26*). Ideally, a label-free noninvasive portable device is needed in the operating room. In particular, the device is designed for easy intraoperative navigation and real-time imaging. The combination of high-resolution, fast and portable PAI will enable accurate diagnosis

and resection for micrometastasis tumors. Further development of the device will imply PAI guided tumor surgeries improvement and patient prognosis in the future (*27*).

Here, we conducted a comprehensive study to accurately detect tumor micrometastases in living animals and clinical samples without labeling by high-resolution PAI systems (Fig. 1). Our results showed that PAI technique is comparable with conventional imaging technologies such as MRI and PET to some extent, permitting clinical applications for early diagnosis of tumor and guiding intraoperative resection.

MATERIALS AND METHODS

Additional full protocols for animal model preparation, bioluminescence imaging, MRI and PET/CT, clinical samples collection and analysis, and histopathology are provided in the supplemental materials. The study timeline is shown in the Supplemental Figure 1.

PAI of Hepatic Melanoma Mouse In Vivo

A pulse laser integrated with a high-frequency ultrasound system (Vevo LAZR-X, VisualSonics, FujiFilm, Japan), holding the advantages of fast imaging and portability, was used to simultaneously acquire photoacoustic and ultrasound images (*28*). A tunable laser (680-970 nm) with repetition rate of 20 Hz was integrated into a 256-element linear array with a main frequency of 40-MHz. ultrasound/photoacoustic signals were processed and reconstructed in a work station. The energy supplied by each pulse of the tunable laser was, 1.2 mJ/cm^2, well below the standard set by American National Standard Institute across the wavelength range. Before imaging, the mice were evenly smeared with medical ultrasound couplant on the target areas and placed on the heating stage connected with an anesthetic catheter. The 3D scanning was controlled by an electric motor with a self-driven step size of 0.14 mm. Oxygen saturation (sO_2) images were acquired at 750 and 850 nm, then analyzed by Vevo LAB tool (VisualSonics, FujiFilm, Japan). The 3D area (>30 slices) was analyzed by tracking the region of interest. Linear least squares spectral

decomposition algorithm was used to calculate the absorption of endogenous melanin in the liver relative to the total photoacoustic signal (*29*). The contrasting images of melanin and hemoglobin were obtained on account of their distinct absorption spectra.

A hemispherical PAI system (Nexus 128, Endra, MI) was used to acquire high-resolution images (*30*). The system consists of a tunable laser beam (680-950 nm) with a frequency of 20 Hz and 128 ultrasonic transducers of frequency 5 MHz that are evenly arranged on the surface of a hemispherical bowl. The laser beam irradiates from the bottom of the bowl and is amplified by a concave lens. A custom-made tray with a round slot in the center was placed on top of the bowl to position the mice, which was confirmed to have a negligible effect on the photoacoustic signal. The bowl and the slot were filled with distilled water to provide acoustic coupling with the imaging target. During imaging, the mice were suitably oriented for optimal alignment. The photoacoustic images were reconstructed and displayed using OsiriX imaging software (OsiriX Foundation) with a maximum-intensity projection (MIP) algorithm. The ratio of the tumor's photoacoustic signal to the background liver's signal was then calculated.

Hematoxylin and Eosin (H&E) Staining and Immunohistochemistry (IHC)

The resected tissues were fixed in 4% paraformaldehyde, embedded in paraffin, and cut into 5 μm sections. For histological examination, the sections were stained with H&E and observed under 5× magnification (Olympus BX51, Japan). Tumor angiogenesis and tumor hypoxic areas were stained with anti-CD31 and anti-pimonidazole antibody respectively by IHC.

In Vivo PAI Guided Surgical Operations

After the melanoma grew to ~4 mm^3, we conducted in vivo simulated surgeries guided by PAI. During the surgical simulation, the nude mouse was placed on a mouse table for position adjustment and then anesthetized with 2-4% isoflurane. For simulated melanoma resection surgery monitoring, we used operating scissors, forceps, suture

needle, and a surgery needle. The simulated melanoma resection surgery was performed in seven steps: photoacoustic image-guided skin incision, melanoma detection, and imaging (step 0), the advancement of the needle towards tumor (step 1-5), photoacoustic image-guided melanoma partial resection (step 6), PAI detecting residual tumor and completing resection (step 7) and skin suturing.

Statistical Analysis

All data analysis was performed using the Statistical Product and Service Solutions software package (version 21.0, IBM Corp., Armonk, NY, USA). Data are presented as the mean ± standard error mean. Two-tailed paired t test was used to compare the changes in photoacoustic and PET signals in metastasized tumors.

RESULTS

PAI of Hepatic Melanoma In Situ

Mice bearing melanoma in the liver were longitudinally monitored at 780 nm before, and from the 4th till 14th day after model establishment to evaluate the feasibility of portable PAI in hepatic melanoma. As shown in Fig. 2A, the normal liver displayed low homogeneous background signal. On the 7th day after melanoma cells injection, a 4.5 times brighter photoacoustic signal ‘dot’ (indicated by the yellow arrow) appeared, likely generated by the incipient tumor. The photoacoustic signal ratios of the tumor to that of the adjacent healthy tissue increased to 6.7 and 9.9 on day 10 and day 14 respectively, corresponding to the growing tumor mass. The results showed that PAI detected hepatic tumor masses of diameter as small as ~400 μm depicted in Fig. 2A. By taking advantage of the distinct absorption spectra of melanin and hemoglobin (Fig. 2B), the visualization of hepatic melanoma growth (green) against a background of liver (red) was realized by multi-wavelength PAI at 680, 730, 924, and 950 nm (Fig. 2A). The photoacoustic signals displayed were consistent with the unmixed pseudo-green signal in Figure 2A, which were further validated as a small tumor by H&E staining (Fig. 2C). 3D view displayed the

morphological changes of the whole tumor (Fig. 2A). Supplemental Videos 1-3 showed the reconstructed 3D views of the invasive metastatic tumor in the liver on days 7, 10, and 14 respectively. The time-dependent increase in volume indicated irregular and invasive growth of the tumor, which agreed well with the increasing intra-tumoral photoacoustic signal (Fig. 2B). Moreover, the detecting limit of PAI was ~219 cells in phantom (*31*) (Supplemental Fig. 2) and imaging depth of ~7 mm was displayed in vivo (Supplemental Fig. 3). Taken together, PAI is a non-invasive, highly sensitive and high-contrast imaging tool that can detect submillimeter scale tumors at the early stages, and is a feasible option for direct long-term surveillance.

Comparison of Different Imaging Techniques for Hepatic Metastasis of Melanoma

To determine the potential clinical value of PAI, we compared it with ultrasound, MRI, bioluminescence imaging, and ^{18}F-FDG-PET/CT on the melanoma hepatic metastasis model. PAI detected the metastatic tumors by the 6th day after modeling (yellow arrows) and was synchronously validated by bioluminescence imaging (Fig. 3). Three orthogonal views and 3D photoacoustic images of the metastatic tumors are shown in Supplemental Figure 4. Ultrasonic imaging of the liver showed even echo signals while the metastatic tumors displayed low heterogeneous signals on the 9th day (Fig. 3). T2-weighted MRI of the same axial plane also showed high signal intensity of the tumors against a dark homogeneous liver background on the 9th day (Fig. 3). Thus, PAI detected hepatic metastases significantly much earlier compared to the conventional imaging modalities. PAI also monitored the process of tumorigenesis from engraftment to oncogenesis (Supplemental Fig. 5) and monitored tumorigenesis on day 6, suggesting that PAI may be a visualization tool for early tumorigenesis.

Furthermore, as shown in Figure 4A, both PAI with ^{18}F-FDG-PET/CT detected tumorigenesis in vivo. However, while PAI distinguished every single tumor with the exact size and location, ^{18}F-FDG-PET only indicated the presence of tumors. The number of

tumors (Fig. 4B) was increasing from day 5 to day 14. The photoacoustic signal ratios of the melanoma hepatic metastasis to the ambient normal liver tissue were ~2.3 and ~2.1 times higher than that of ^{18}F-FDG-PET on day 8 and day 14 respectively (Fig. 4B). Supplemental Videos 4 and 5 showed multiple views of the metastatic tumors, and the changes in their morphology in three dimensions at 1 and 2 weeks. These results indicated that PAI showed high sensitivity and resolution in screening melanoma hepatic micrometastases.

Monitoring of Oxygenation Dynamics in Metastatic Hepatic Carcinoma with PAI

Functional imaging of PAI could not only detect pharmacokinetics through ICG (Supplemental Fig. 6), but also evaluate sO_2 metabolism without labeling. As shown in Figure 5A, the tumors showed a gradual increase in sO_2 with clear boundaries against a homogeneous background of the liver. However, the intra-tumoral change in sO_2 was inconsistent due to heterogeneous tumor growth (*32*), with lower levels in the center compared to the margin. Average sO_2 that was integrally quantified was constantly increasing till day 10. Positive immunostaining of CD31 in the tumor tissue sections confirmed angiogenesis and the quantitative of tumor angiogenesis showed an increasing trend (Fig. 5B). These suggested that require oxygen for the proliferating tumor cells with high metabolic rates was supplied by angiogenesis. The gradient of sO_2 showed a downward trend, implying that a small number of tumor cells may have hypoxia. Positive immunostaining of pimonidazole in the tumor tissue sections also confirmed tumor cells hypoxia and the quantitative of hypoxic areas showed an increasing trend (Fig. 5B). The panoramic views of stained tumor sections were shown (Supplemental Fig. 7). These results indicated that PAI can be used to detect sO_2 and oxygen metabolism in the tumors, which are valuable parameters to establish the therapeutic regimen and make clear prognostic assessment (*33*).

Detection of Clinical and Preclinical Samples by PAI

Experimental results for clinical samples from 9 patients with primary hepatic carcinoma were shown in Figure 6A. The first row showed the photograph of tumor tissue in ambient normal tissue. PAI images for the samples were shown in the second row. The margins of the tumor and normal tissue were determined by bright photoacoustic signal due to blood chromophores with optical absorption properties. Meanwhile, the histological results were depicted in the third row for the tumor and normal tissue. In addition, tumor tissues from stomach, colorectum, and esophagus were imaged by PAI (Supplemental Figs. 8 and 9), which showed better depth imaging (Supplemental Fig. 10). The grayscale photoacoustic images were analyzed to determine the tumor boundaries (Supplemental Fig. 11) and signal distribution (Supplemental Figs. 12 and 13). The results for preclinical samples from mouse hepatic metastatic melanoma were displayed in Figure 6B**.** Photographs of metastatic melanoma from frozen sections were consistent with melanoma signals from PAI. Therefore, our results suggested that PAI is potential for detection tumor and guiding tumor surgery.

PAI Guided Surgery of Hepatic Metastases

We further examined the intraoperative guidance ability of PAI, as shown by the 2D images in Figure 7. A preoperative PAI was first performed to determine the tumor location (step 0). A typical reconstructed 3D image of the metastatic tumor is shown, which provided profile of the tumor in the surgical region to surgeon. The surgical margin was then obviously indicated using a steel needle (step 1). The needle and the tumor were clearly visible as the needle continually advanced to the tumor boundary with its movement shown in steps 2-5 and Supplemental Video 6. We initially performed a partial resection with PAI guidance, and the residual tumor is shown in step 6. The tumor was completely resected subsequently without residue detected in step 7. Ex vivo liver lobes were stacked by inserting a needle into the upper lobe and placed in the tray and imaged at 780 nm. The maximum imaging depth reached 11 mm with satisfied contrast

(Supplemental Fig. 14). Taken together, intraoperative PAI can effectively locate tumors, identify residual masses, and guide surgical resection.

DISCUSSION

We used novel PAI technology to detect micrometastatic melanoma in the liver of live mice. The PAI system integrates high temporal and spatial resolution, deep penetration, multiple contrasts, and high sensitivity, therefore can capture structural and functional images of small animals. As a completely non-invasive, fast imaging technique, it is also suitable for long-term monitoring. Our results demonstrated that PAI had the ability to monitor tumor volume changes and metastatic nodes, which opened a new window for medical researchers to treat and diagnose patients without the danger of ionizing radiation in CT or PET/CT (*34*). Alternatively, PAI could be used as a visualization tool for early stage in tumor formation of liver. Moreover, it clearly distinguished the blood vessels and liver of mice, which could be used to directly diagnose pathological changes in liver.

We illustrated the formation process of micro tumors by PAI and established a tool for quantitative evaluation of micrometastasis. PAI could detect microscopic melanoma as small as ~400 μm in vivo and melanoma cells as few as ~219 in vitro. We detected micro tumors in vivo using PAI technology, which had stronger photoacoustic signal than that before inoculation. In contrast, neither ultrasound nor MRI was able to detect any changes in the liver at early stage. Therefore, PAI is an effective tool for the quantitative evaluation of micrometastasis and can be used as a complementary modality to ultrasound, MRI, and PET.

Tumor development is accompanied by microvessel regeneration and local hypoxia. Assessing the hemodynamic responses to oxygen is an effective means to monitor tumor metabolism (*35*). Using different wavelengths, PAI achieved functional imaging in tumor of mouse liver. The results demonstrated that the increase in sO_2 during tumor growth is presumed to be due to the tumor micro vessel in the early stage *(36)*. The decrease in the

gradient of sO_2 suggested that it may be attributable to the occurrence of hypoxia in the tumor (*21,37*). In addition, PAI showed the process of pharmacokinetics in both the mouse liver and internal organs with the assistance of ICG (*38*). Further clinical application of PAI is conceivable and is being actively carried out, for example, to design optimal dosing regimens and administration.

Previous studies have shown that PAI can identify tumors located beneath the surface of the normal brain tissue and even guide the resection of larger tumors (*26*). Our portable PAI was able to visualize tumor location and excision in real time during the operation, as well as any residual cancer tissue within the incision margin post-resection. Therefore, portable PAI is a highly promising technique that can provide visual guidance during surgery. In addition, intraoperative PAI can potentially detect deeper tumors, and improve their detection as well as complete resection rate.

The feasibility of PAI system in the surgical environment was successfully evaluated by in vivo surgery, including image-guided melanoma excision. However, the following improvements are necessary for future clinical applications: (1) the ability to monitor the movement of surgical instruments in the deeper layers of the tissues by changing the material of the needle. For example, ceramic scalpels may be used for PAI during surgery (*39,40*). (2) greater imaging depth which can be achieved by increasing the laser power, and (3) miniaturization of the photoacoustic probe with adequate signal sensitivity in order to allow sufficient operation space.

CONCLUSION

PAI as a new imaging method with high sensitivity and specificity can monitor the micro-tumors (<1 mm) which cannot be detected by traditional imaging techniques, realizing the early diagnosis of tumors and guiding doctors to make treatment plans as early as possible. Under precise detection conditions, PAI can be further developed to help guide tumor resections by reducing residues. Although this study focuses on melanoma

hepatic metastasis, we believe that this method can be extended to other tumors, such as glioma and breast cancer.

DISCLOSURE

This work was supported by the National Science Foundation of China (81922034, 91859113&81571744), the Fundamental Research Funds for the Central Universities (20720170065), the Science Fund for Distinguished Young Scholars of Fujian Province (2018J06024), and the Science Foundation of Fujian Province (No. 2014Y2004). No potential conflicts of interest relevant to this article exist.

ACKNOWLEDGMENTS

Q. Y., S. H., and L. N. conceived and designed the research project. S. H., Q. Y., and Z. W. performed the experiments and data analysis. J. Z. provided the sample of human cancer. S. H., Q. Y., X. C., and L. N. wrote the manuscript. L. N. supervised the entire study. All authors proofread the manuscript.

KEY POINTS

QUESTION: Can PAI be used as a label-free, noninvasive and nonionization biomedical imaging modality for early detection of deep tumor hepatic micrometastasis and guiding tumor resection as an affordable and clinically friendly technology?

PERTINENT FINDINGS: Our study showed that PAI could achieve a label-free and noninvasive detection of small (~400 μm) and deep (~7 mm) tumors in vivo and surgical resection of submillimeter tumors based on PAI with structural and functional imaging features, which was verified by histopathological methods.

IMPLICATIONS FOR PATIENT CARE: PAI, a robust surveillance technique, provides rapid, label-free and noninvasive detection with high resolution and sensitivity,

which can guide surgical removal of submillimeter tumors to improve patient outcomes in the future.

REFERENCES

1. Siegel RL, Miller KD, Jemal A. Cancer statistics, 2017. *CA Cancer J Clin.* 2017;67:7-30.
2. Chambers AF, Groom AC, MacDonald IC. Dissemination and growth of cancer cells in metastatic sites. *Nat Rev Cancer.* 2002;2:563-572.
3. Welch DR, Hurst DR. Defining the hallmarks of metastasis. *Cancer Res*. 2019;79:3011-27.
4. Neuschmelting V, Lockau H, Ntziachristos V, Grimm J, Kircher MF. Lymph node micrometastases and in-transit metastases from melanoma: in vivo detection with multispectral optoacoustic imaging in a mouse model. *Radiology.* 2016;280:137-150.
5. Agarwala SS, Eggermont AM, O'Day S, Zager JS. Metastatic melanoma to the liver: a contemporary and comprehensive review of surgical, systemic, and regional therapeutic options. *Cancer.* 2014;120:781-789.
6. Carreno BM, Garbow JR, Kolar GR, et al. Immunodeficient mouse strains display marked variability in growth of human melanoma lung metastases. *Clin Cancer Res.* 2009;15:3277-3286.
7. Tawbi HA, Forsyth PA, Algazi A, et al. Combined nivolumab and ipilimumab in melanoma metastatic to the brain. *N Engl J Med.* 2018;379:722-730.
8. Einhorn LH, Burgess MA, Gottlieb JA. Metastatic patterns of choroidal melanoma. *Cancer.* 1974;34:1001-1004.
9. Pawlik TM, Zorzi D, Abdalla EK, et al. Hepatic resection for metastatic melanoma: distinct patterns of recurrence and prognosis for ocular versus cutaneous disease. *Ann Surg Oncol.* 2006;13:712-720.
10. Balch CM, Soong SJ, Gershenwald JE, et al. Prognostic factors analysis of 17,600 melanoma patients: validation of the American Joint Committee on Cancer melanoma staging system. *J Clin Oncol.* 2001;19:3622-3634.

11. Mehlen P, Puisieux A. Metastasis: a question of life or death. *Nat Rev Cancer.* 2006;6:449-458.
12. Sahani DV, Bajwa MA, Andrabi Y, Bajpai S, Cusack JC. Current status of imaging and emerging techniques to evaluate liver metastases from colorectal carcinoma. *Ann Surg.* 2014;259:861-872.
13. Wang LV, Wu H-i. *Biomedical optics: principles and imaging.* Hoboken, NJ: Wiley; 2007: 283-284.
14. Wang LV, Hu S. Photoacoustic tomography: in vivo imaging from organelles to organs. *Science.* 2012;335:1458-1462.
15. Liu Y, Nie L, Chen X. Photoacoustic molecular imaging: from multiscale biomedical applications towards early-stage theranostics. *Trends Biotechnol.* 2016;34:420-433.
16. Staley J, Grogan P, Samadi AK, Cui H, Cohen MS, Yang X. Growth of melanoma brain tumors monitored by photoacoustic microscopy. *J Biomed Opt.* 2010;15:040510.
17. Wang B, Su JL, Amirian J, Litovsky SH, Smalling R, Emelianov S. Detection of lipid in atherosclerotic vessels using ultrasound-guided spectroscopic intravascular photoacoustic imaging. *Opt Express.* 2010;18:4889-4897.
18. Viator JA, Komadina J, Svaasand LO, Aguilar G, Choi B, Stuart Nelson J. A comparative study of photoacoustic and reflectance methods for determination of epidermal melanin content. *J Invest Dermatol.* 2004;122:1432-1439.
19. Stoffels I, Morscher S, Helfrich I, et al. Metastatic status of sentinel lymph nodes in melanoma determined noninvasively with multispectral optoacoustic imaging. *Sci Transl Med.* 2015;7:317ra199.
20. Li L, Zhu L, Ma C, et al. Single-impulse panoramic photoacoustic computed tomography of small-animal whole-body dynamics at high spatiotemporal resolution. *Nat Biomed Eng.* 2017;1.

21. Yao J, Maslov KI, Zhang Y, Xia Y, Wang LV. Label-free oxygen-metabolic photoacoustic microscopy in vivo. *J Biomed Opt.* 2011;16:076003.
22. Frangioni J. In vivo near-infrared fluorescence imaging. *Curr Opin Chem Biol.* 2003;7:626-634.
23. Kularatne SA, Thomas M, Myers CH, et al. Evaluation of novel prostate-specific membrane antigen-targeted near-infrared imaging agent for fluorescence-guided surgery of prostate cancer. *Clin Cancer Res.* 2019;25:177-187.
24. Wilson KE, Bachawal SV, Willmann JK. Intraoperative resection guidance with photoacoustic and fluorescence molecular imaging using an anti-B7-H3 antibody-indocyanine green dual contrast agent. *Clin Cancer Res.* 2018;24:3572-3582.
25. Wong TTW, Zhang R, Hai P, et al. Fast label-free multilayered histology-like imaging of human breast cancer by photoacoustic microscopy. *Sci Adv.* 2017;3:e1602168.
26. Kircher MF, de la Zerda A, Jokerst JV, et al. A brain tumor molecular imaging strategy using a new triple-modality MRI-photoacoustic-Raman nanoparticle. *Nat Med.* 2012;18:829-834.
27. Moore C, Jokerst JV. Strategies for image-guided therapy, surgery, and drug delivery using photoacoustic imaging. *Theranostics.* 2019;9:1550-1571.
28. Wu Z, Duan F, Zhang J, Li S, Ma H, Nie L. In vivo dual-scale photoacoustic surveillance and assessment of burn healing. *Biomed Opt Express.* 2019;10:3425-3433.
29. Kim S, Chen YS, Luke GP, Emelianov SY. In vivo three-dimensional spectroscopic photoacoustic imaging for monitoring nanoparticle delivery. *Biomed Opt Express.* 2011;2:2540-2550.
30. Lv J, Peng Y, Li S, et al. Hemispherical photoacoustic imaging of myocardial infarction: in vivo detection and monitoring. *Eur Radiol.* 2018;28:2176-2183.

31. Neuschmelting V, Lockau H, Ntziachristos V, Grimm J, Kircher MF. Lymph node micrometastases and in-transit metastases from melanoma: in vivo detection with multispectral optoacoustic imaging in a mouse model. *Radiology.* 2016;280:137-150.
32. Reina-Campos M, Moscat J, Diaz-Meco M. Metabolism shapes the tumor microenvironment. *Curr Opin Cell Biol.* 2017;48:47-53.
33. Menon C, Fraker DL. Tumor oxygenation status as a prognostic marker. *Cancer Lett.* 2005;221:225-235.
34. Hong H, Zhang L, Xie F, et al. Rapid one-step ^{18}F-radiolabeling of biomolecules in aqueous media by organophosphine fluoride acceptors. *Nat Commun*. 2019;10:989.
35. Skala MC, Fontanella A, Lan L, Izatt JA, Dewhirst MW. Longitudinal optical imaging of tumor metabolism and hemodynamics. *J Biomed Opt.* 2010;15:011112.
36. Nie L, Huang P, Li W, et al. Early-stage imaging of nanocarrier-enhanced chemotherapy response in living subjects by scalable photoacoustic microscopy. *ACS Nano.* 2014;8:12141-12150.
37. Gerling M, Zhao Y, Nania S, et al. Real-time assessment of tissue hypoxia in vivo with combined photoacoustics and high-frequency ultrasound. *Theranostics.* 2014;4:604-613.
38. Taruttis A, Morscher S, Burton NC, Razansky D, Ntziachristos V. Fast multispectral optoacoustic tomography (MSOT) for dynamic imaging of pharmacokinetics and biodistribution in multiple organs. *PLoS One.* 2012;7:e30491.
39. Klocke F, Linke B, Schluetter D. Development of a reliable grinding procedure for ceramic medical instruments. *Production Engineering*. 2010;4:571-579.
40. Burbelo RM, Gulyaev AL, Robur LI, Zhabitenko MK, Atamanenko BA, Kryl YA. Photoacoustic visualization of residual stress in ceramic material. *Le Journal de Physique IV*. 1994;04:C7-311-C317-314.

Figure legends

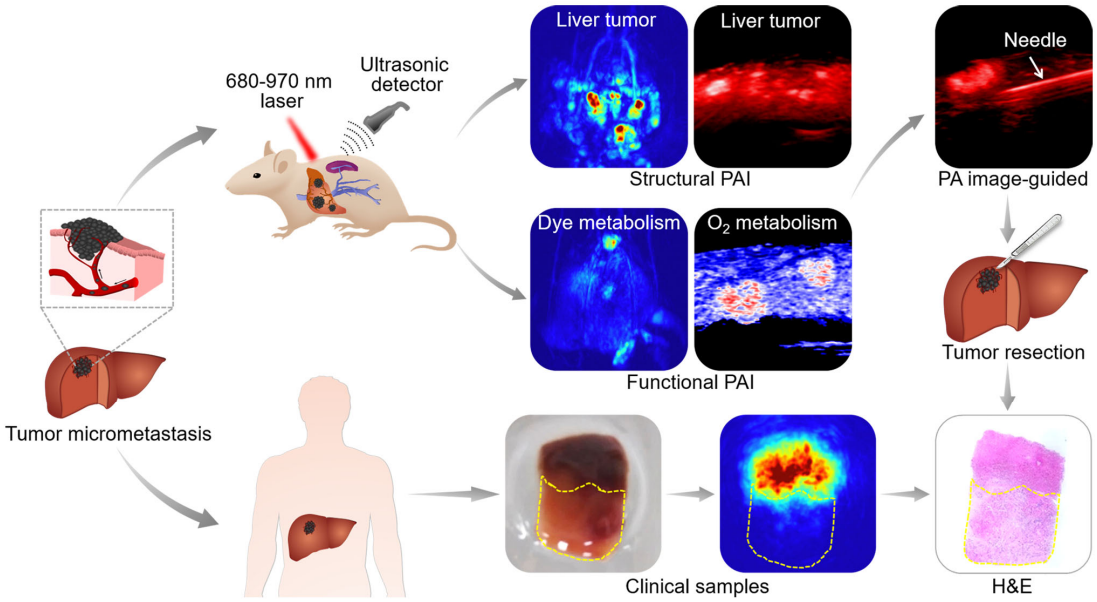

FIGURE 1. Workflow of PAI for melanoma hepatic metastasis detection, profiling, and resection for animal models and clinical samples. Two kinds of tumor hepatic metastasis models were established by injecting B16 tumor cells directly into the mouse hepatic lobe and subcapsular of the spleen. B16 cells entered the liver tissue through the hepatic portal vein and developed into tumors. Tumor samples were used for PAI and pathologically verified.

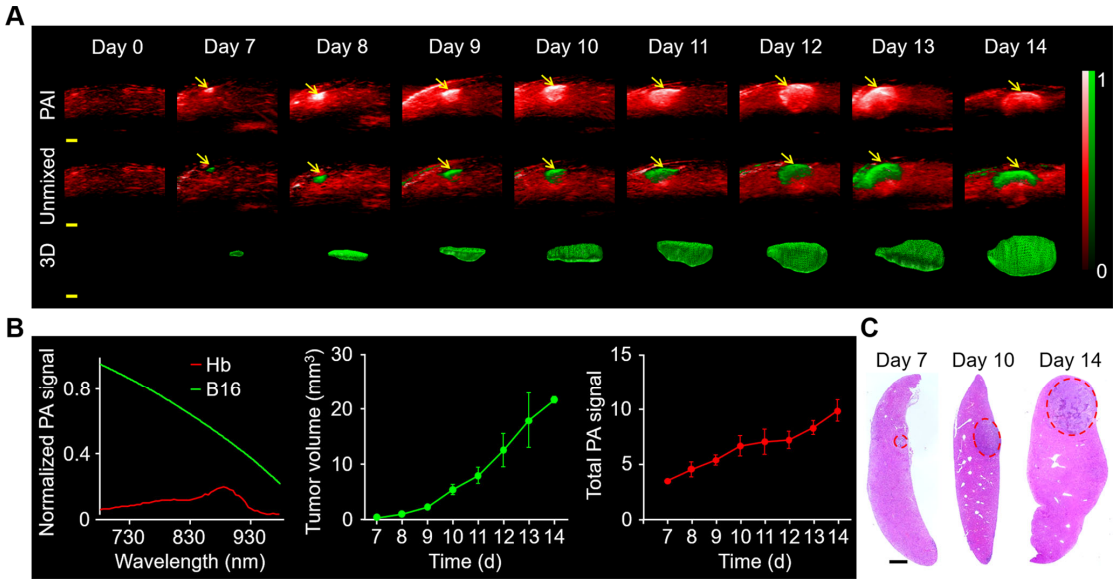

FIGURE 2. PAI displays changes for hepatic melanoma in situ. (A) *In vivo* PAI of liver before and after hepatic melanoma modeling by hepatic injection at 780 nm (n = 3). Melanoma (green) and hemoglobin (red) were unmixed by multi-wavelength photoacoustic imaging at 680, 730, 924, and 950 nm. 3D view of the tumors were shown. Scale bars in all images were 1 mm. (B) Normalized PA signal spectra of hemoglobin and B16. Measurement of tumor volume and PA signal by PAI. (C) H&E of the tumor at different time points. Scale bars in histological images were 1 mm. PA = photoacoustic.

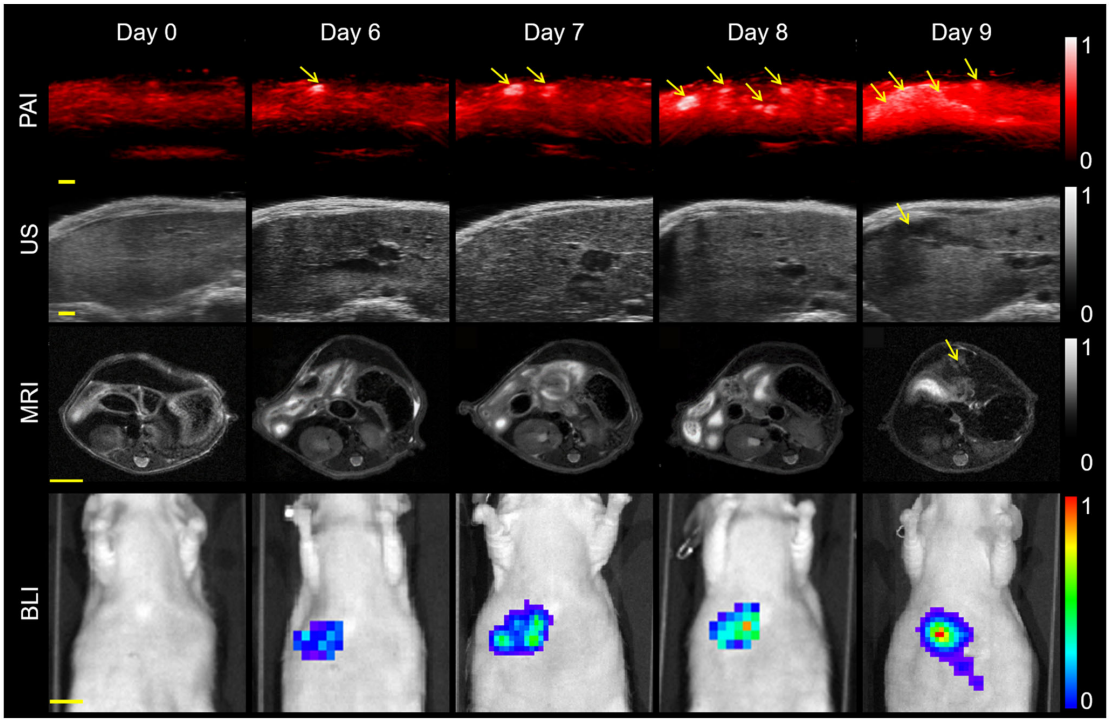

FIGURE 3. Comparison of various imaging modalities. PA, US, bioluminescence and MR imaging of the melanoma hepatic metastasis model mouse at different days after tumor cells injection in the spleen. The hepatic metastases could be found in the PAI, US, and MRI on the day 6, day 9, and day 9, respectively. The excitation wavelength was 780 nm. Scale bars in PA and US images were 1 mm. Scale bars in MR and bioluminescence images were 5 and 10 mm, respectively. PA = photoacoustic; MR = magnetic resonance; US = ultrasound.

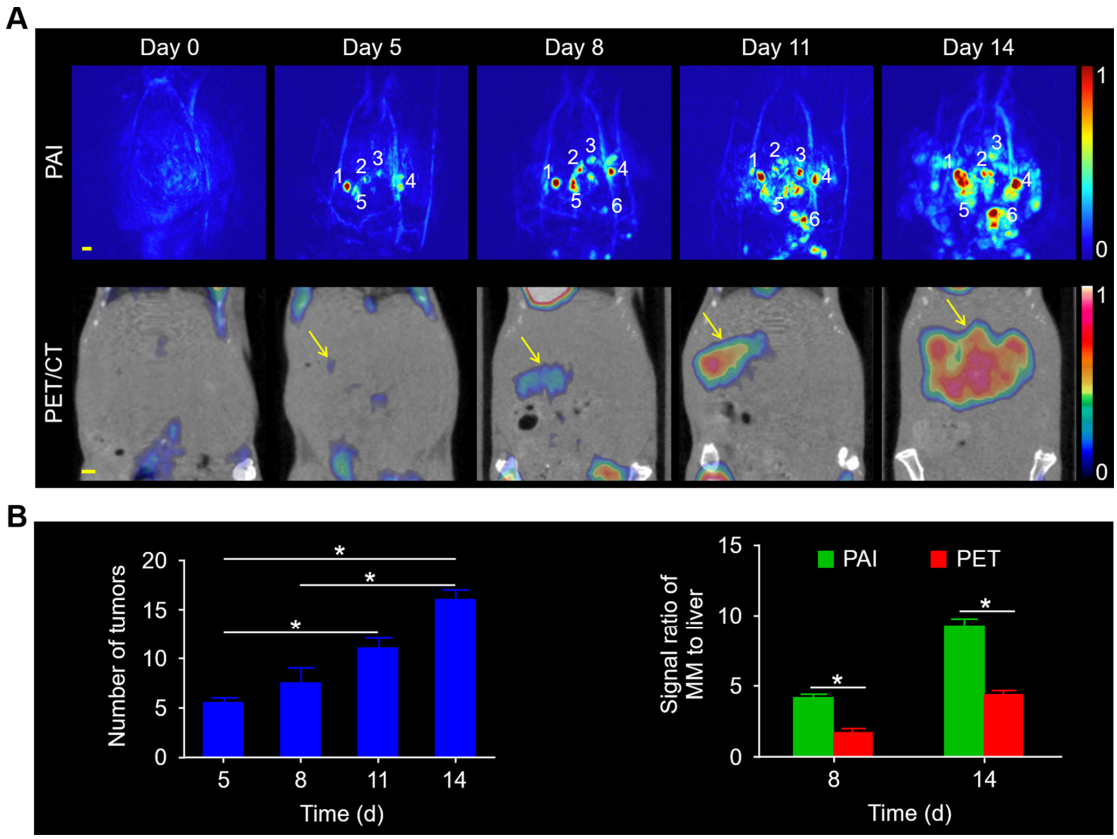

FIGURE 4. PAI and PET for melanoma hepatic metastasis mice. (A) PAI and PET/CT imaging of the melanoma hepatic metastasis mouse at different days after tumor cells injection with 3 days interval. Scale bars in all images were 1 mm. (B) The number of tumors over time was counted. Signal ratio of melanoma hepatic metastases to liver was quantified in PAI and PET after 8 days and 14 days of tumor cells injection. MM = melanoma metastasis.

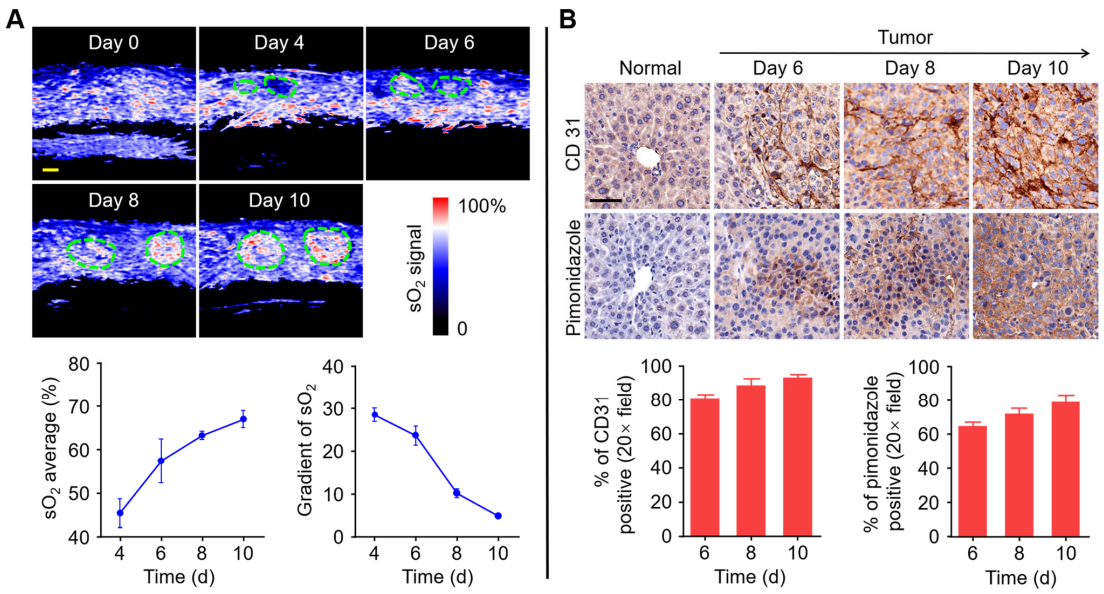

FIGURE 5. Functional parameters monitoring in tumor and normal tissue. (A) The change of tumor blood oxygenation increased from day 4 to day 10. Region of interest represents the tumor. Scale bars in sO_2 images were 1 mm. sO_2 average and gradient of sO_2 were quantified respectively. (B) Representative IHC images of slices collected from normal and melanoma mice liver after day 6, day 8, and day 10 post injection B16 cells. The nuclei, tumor angiogenesis, and tumor hypoxic areas were stained with hematoxylin, anti-CD31 antibody, and anti-pimonidazole antibody, respectively. Scale bars in IHC images were 50 μm. Tumor angiogenesis and hypoxic areas from IHC images were quantified.

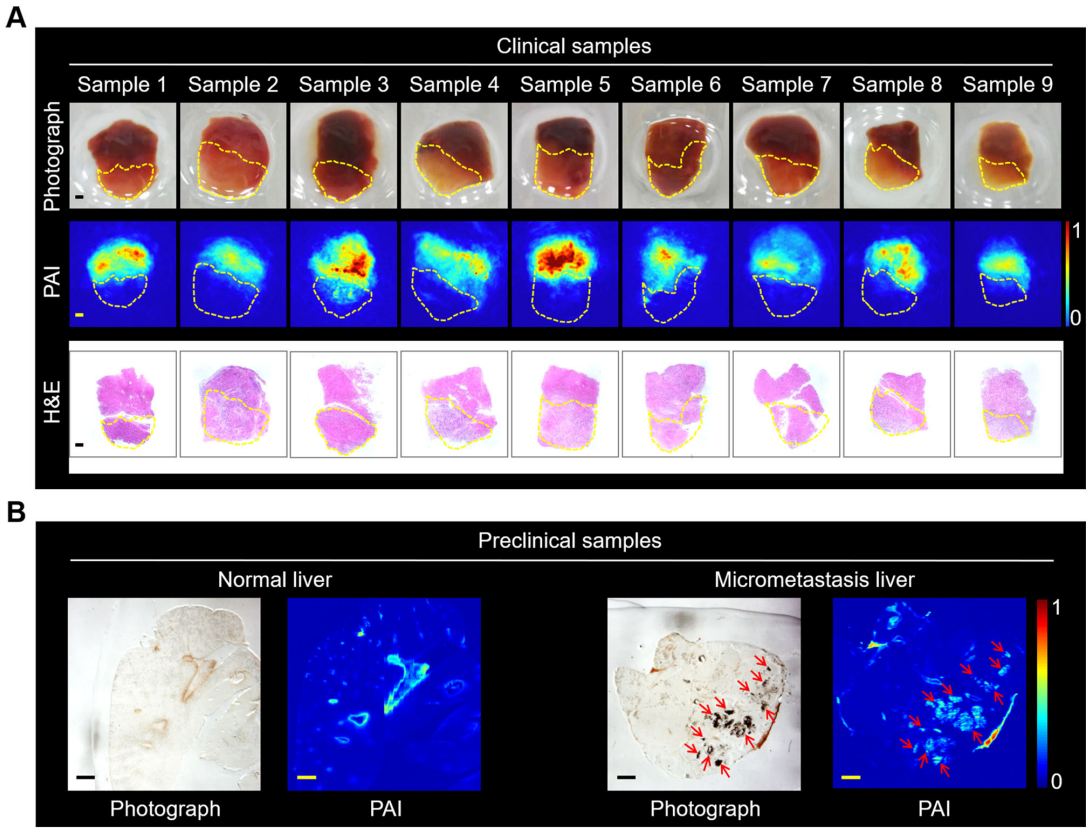

FIGURE 6. PAI of clinical and preclinical samples. (A) Tumor samples from 9 patients were used for photographing, PAI, and H&E staining. Region of interest represents the tumor. Scale bars in clinical sample images were 1 mm. (B) Photographs and PAI of normal and melanoma micrometastasis liver slices. The red arrow represents the tumor. The thickness of liver slice is 50 μm. Scale bars in preclinical sample images were 1 mm. MM = melanoma metastasis.

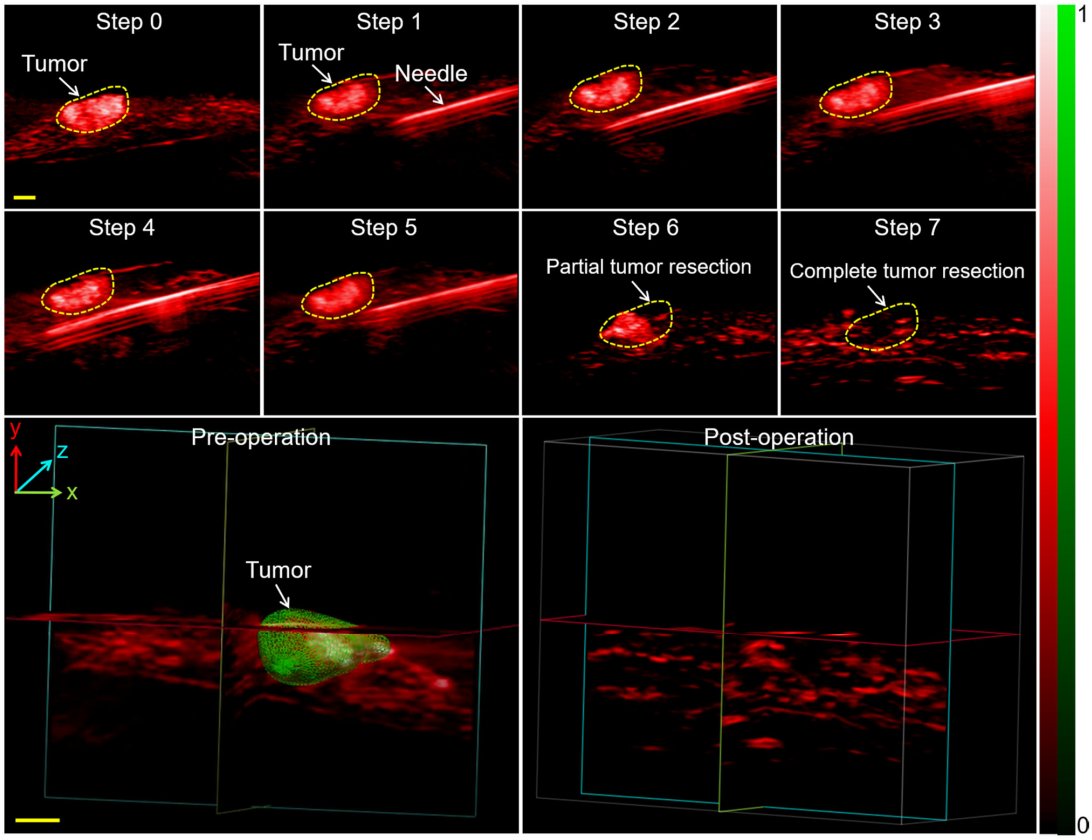

FIGURE 7. Needle insertion and photoacoustic image-guided tumor resection *in vivo*. Photoacoustic images of metastatic tumor after laparotomy (step 0), the advancement of the needle towards tumor (step 1-5), partial resection (step 6) and complete resection (step 7) with photoacoustic guiding. Three-dimensional photoacoustic images before and after resection were displayed. 3D melanoma (green) and hemoglobin (red) distributions were estimated by spectral unmixing analyses from spectroscopic acquisitions at 680, 730, 924, and 950 nm, respectively. Scale bars in all images were 1 mm.

SUPPLEMENTAL MATERIALS

Cell Lines and Culture

Luciferase-expressing melanoma B16 and hepatoma HepG2 cell lines were maintained in Dulbecco's modified eagle medium (DMEM; Sigma-Aldrich, St. Louis, MO, USA) supplemented with 10% fetal bovine serum (FBS; Sigma-Aldrich), 100 U/ml penicillin and 100 mg/ml streptomycin, at 37 °C with 5% CO_2. One hour prior to injecting into mice, 90-100% confluent cultures were harvested by trypsinization (0.25% trypsin and 0.02% ethylene diamine tetraacetic acid in sterile phosphate buffer, PBS), and re-suspended in the sterile PBS to final densities.

Establishment of Tumor Xenografts

All animal experiments were performed in accordance with the relevant guidelines and regulations. The study protocols were approved by the Ethical Committee for Animal Research at Xiamen University. Six- to eight-week-old male immunodeficient nude mice were purchased from the Laboratory Animal Center of Xiamen University. During the experiments, the animals were anesthetized with 2-4% isoflurane and placed on an electric temperature-controlled heating plate. The primary liver xenograft was established by injecting 2×10^6 HepG2 cells directly into the hepatic lobe. The metastasis models were established by injecting 2×10^6 B16 cells either into the left hepatic lobe (in 10 μL PBS) or the subcapsular spleen (in 50 μL PBS). The hepatic lobe and spleen were exteriorized through a 5 mm incision below the xiphoid or in the left abdomen above the spleen respectively. The cells were injected into the hepatic or splenic parenchyma using a 1 mL syringe fitted with a 29 G needle. The incision was closed using absorbable sutures.

The mice were imaged 4 days after tumor cells injection. A mixture of 5% isoflurane in air was used to anesthetize the animals. The anesthetic state was maintained with 2% isoflurane and monitored by the respiration rate (25-30 breaths per minute). The mice were euthanized when the tumor was larger than 1 cm in diameter, or when the animals

displayed tumor-related symptoms such as signs of pain, bleeding, ulcers, necrosis, or weight loss.

In Vitro Experiments and PAI of B16 Cells

The tissue-mimicking agarose phantom was made using a cylindrical glass bottle (3 cm^2 cross section × 10 cm length). The phantom consisted of 1.5% agarose per volume and 20% intralipid was added during the cooling process before solidification to mimic tissue scattering and absorption properties. Prior to in vivo imaging, the B16 cell suspensions of varying numbers (0, 2.19×10^2, 3.5×10^2, 4.38×10^2, 8.75×10^2, 1.75×10^3, 3.5×10^3, 1.75×10^4, and 3.5×10^4) in 10 μL PBS were imaged to determine the imaging sensitivity. The cells were embedded in a tissue-mimicking phantom (n = 3 for each) and imaged photoacoustically at 780 nm.

MRI of Hepatic Metastasis Mouse In Vivo

MRI was performed on a Bruker Biospin 9.4 T small animal MRI scanner (Bruker, Germany) equipped with a horizontal bore (diameter, 30 cm; gradient strength, 734 mT/m), and fitted mouse body coil. T2-weighted axial images were obtained using a spin echo multiple slice sequence with the following parameters: repetition time (TR) = 2500 ms, echo time (TE) = 33 ms, matrix = 256 × 256, field of view (FOV) = 3 × 3 cm^2, signal averaging = 4, section thickness = 1 mm.

BLI of Melanoma Hepatic Metastasis Mouse In Vivo

BL images were obtained using the IVIS® in vivo imaging system (Lumina, Perkin Elmer, USA), which consists of a charge-coupled device (CCD) camera to capture both visible light and luminescent images and an adjustable imaging platform assembled in a light-tight box. The mice were intraperitoneally injected with D-luciferin (150 mg/kg) (Thermo Fisher Scientific, Pittsburgh, PA, USA) 10 min before imaging, and placed on the stage of the imaging chamber. After acquiring the photographic images of each mouse, the

luminescent images were acquired with auto exposure setting. The actual exposure time for a whole mouse was 10 to 30 seconds.

^{18}F-FDG PET/CT Imaging of Melanoma Hepatic Metastasis Mouse In Vivo

Inveon microPET-CT system (Siemens, Germany) was used for whole body imaging. Each mouse was injected with 3.7-7.4 MBq ^{18}F-FDG (PET Center of the First Affiliated Hospital of Xiamen University) of radiochemical purity >98% in a total volume of 50-80 μL through the caudal vein. A static PET/CT scan of the liver was performed on anesthetized mice 40 minutes after ^{18}F-FDG injection. The CT images were acquired by an X-ray camera to determine the orientation of the mice. The PET images were reconstructed using a three-dimensional ordered subset expectation maximization (3D OSEM) algorithm combined with attenuation and scattering correction. The ROI covering the entire tumor was rendered manually on the CT image, and was then applied to the corresponding PET images. The maximum standardized uptake values (SUV_{max}) were calculated for the tumor and normal tissue lesions from the PET images. The ratio of SUV_{max} value of the tumor to that of the normal liver tissue was quantified.

Human Samples Collection and Analysis

Patient tissue collection, PAI and PA image feature extraction. Forty specimens – normal and tumor tissues from the liver, stomach, colorectum and esophagus – were collected from 30 patients who underwent tumor resection at the affiliated Zhongshan Hospital of Xiamen University. Cancer diagnosis had been confirmed pathologically. The samples were collected in accordance to the ethical committee of the Affiliated Zhongshan Hospital of Xiamen University after obtaining written informed consent from each patient.

The tissue samples were flash frozen in liquid nitrogen immediately after excision and divided into three portions for absorption spectroscopy, PAI and histology. Light absorption was measured from 300 to 900 nm with 2 nm increments on identical sample masses after being triturated using Multiskan Spectrum (Thermo Fisher, Germany). PAI

was performed at different wavelengths (700, 750, 800, 850, and 900 nm). Depth imaging was standardized in chicken breast of different thicknesses (0.4, 0.8, 1.2, and 1.6 cm) at 750 nm. The grayscale PA images of the tumors were contoured using Matlab 2018b (MathWorks Inc., US) to determine the boundaries. The dense contours (black arrows) indicated strong tumor infiltration. The signal intensities and distribution in the images were determined by counting the pixels with histograms plotted. Different parameters including kurtosis, skewness, mean, maximum, and minimum were calculated.

Immunohistochemistry (IHC)

The hypoxic area was visualized by IHC using the Hypoxyprobe™-1 Plus Kit (Hypoxyprobe Inc., USA) which detects pimonidazole, a nitroimidazole that selectively accumulates in hypoxic cells and forms stable adducts with protein thiol groups. The tumor-bearing mice were intraperitoneally injected with pimonidazole hydrochloride (60 mg/kg) and sacrificed 1 h later. The tumor tissues were resected and processed as described above. The sections were incubated sequentially with FITC-conjugated mouse anti-pimonidazole monoclonal antibody (dilution 1:200) and peroxidase-conjugated rabbit anti-FITC secondary antibody (dilution 1:200) as per kit instructions. To detect tumor angiogenesis, the tissue sections were probed with rabbit anti-CD31 mouse monoclonal antibody (dilution 1:200, Abcam, UK) and goat anti-rabbit secondary antibody (dilution 1:200, KPL, USA). The sections were counterstained with hematoxylin and observed under 20× magnification. The CD31 or pimonidazole cells were counted in five random fields. The percentages of the respective stained positive cells were calculated using the ImageJ IHC profiler.

Statistical Analysis

The histogram parameters, including kurtosis, skewness, mean, maximum and minimum, were compared between the poorly- and moderately-differentiated tumors using Student's t test. Receiver operating characteristics (ROC) curves were plotted for the above to assess

the area under the curve (AUC). The distinguishing parameters with higher AUC values (range 0.5-1) were identified. P values <0.05 were considered statistically significant.

SUPPLEMENTAL RESULTS

Detection Sensitivity and Imaging Depth Characteristics of PAI

We further evaluated the sensitivity of PAI in terms of detecting cell numbers. In vitro results showed that the detecting limit was ~219 cells (Supplemental Fig. 2A) using current system and the increase in the number of cells was accompanied by an increase in the photoacoustic signal (Supplemental Fig. 2B). Moreover, the PAI could realize maximum imaging depth of ~7 mm in vivo in living mice models of hematogenous metastasis. Three orthogonal planes of maximum-intensity projection (MIP) images taken 2 weeks after modeling were reconstructed by OsiriX. The corresponding coronal, transverse, and sagittal planes of PAI were shown respectively (Supplemental Figs. 3A-3C**)**. As shown in Supplemental Figure 3C, the abdominal vessels (indicated by white arrows marked 'V') and five single tumors (indicated by white arrows marked 'T') were remarkably distinguishable. In the transverse and sagittal views (Supplemental Fig. 3B and 3C), PAI yielded an imaging depth of ~7 mm with a signal to background ratio of 3.3. Taken together, PAI is a non-invasive, highly sensitive and high-contrast imaging tool that can detect submillimeter scale tumors at the early stages, and is a feasible option for direct long-term surveillance.

Pharmacokinetic Monitoring in Primary Liver Cancer with PAI

FDA-approved ICG, which is used to monitor pharmacokinetics of liver and shows significant photoacoustic boost, was selected as contrast agents to obtain better PA signals. We also explored the ability of PAI to monitor the metabolism of primary liver cancer established in a mouse model by subcapsular liver injection of HepG2 cells. The mice were intravenously injected with ICG, which is used to monitor liver function and shows significant photoacoustic boost. As shown in Supplemental Figure 6A, four abdominal

vessels and a homogeneous liver containing a small shadow (enclosed in the red dashed circle) were observed before injecting ICG, while the PA signal of the entire liver was enhanced rapidly within 5 min injection followed by a gradual decrease. After 30 min, the small shadow was conspicuous against the low-signal background, and was validated as a tumor by H&E staining. Meanwhile, the gall bladder (GB) and intestinal tract (IT) were clearly revealed after 5 min of ICG injection due to the biliary excretion of ICG. In addition, agent retention in the GB and IT were significantly longer than those in normal liver and the hepatic tumor. As shown in Supplemental Figure 6B, the time-signal curves of the tumor and liver after ICG injection showed rapid clearance of the latter from the liver (blue line) compared to slower metabolism from the tumor (red line). The PA signal ratio of tumor to liver peaked to ~2.9 after 2 hours. Therefore, PAI can be used to quantify liver metabolic function with the assist of ICG.

SUPPLEMENTAL FIGURES

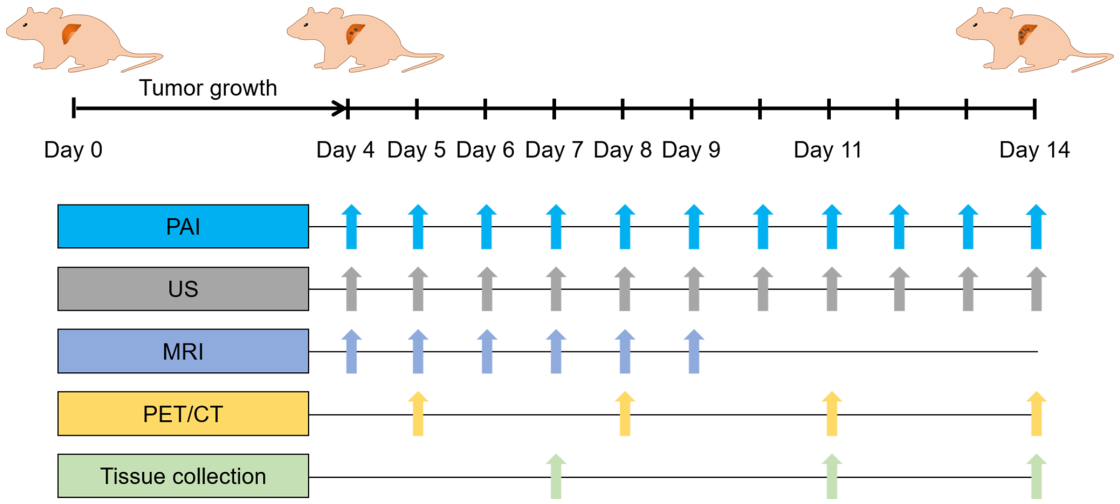

Supplemental Figure 1. Study design of cancer hepatic metastases model for PA, US, MR, and PET/CT imaging in different days. Tissues were collected for pathological and immunohistochemical analysis. PA = photoacoustic; MR = magnetic resonance.

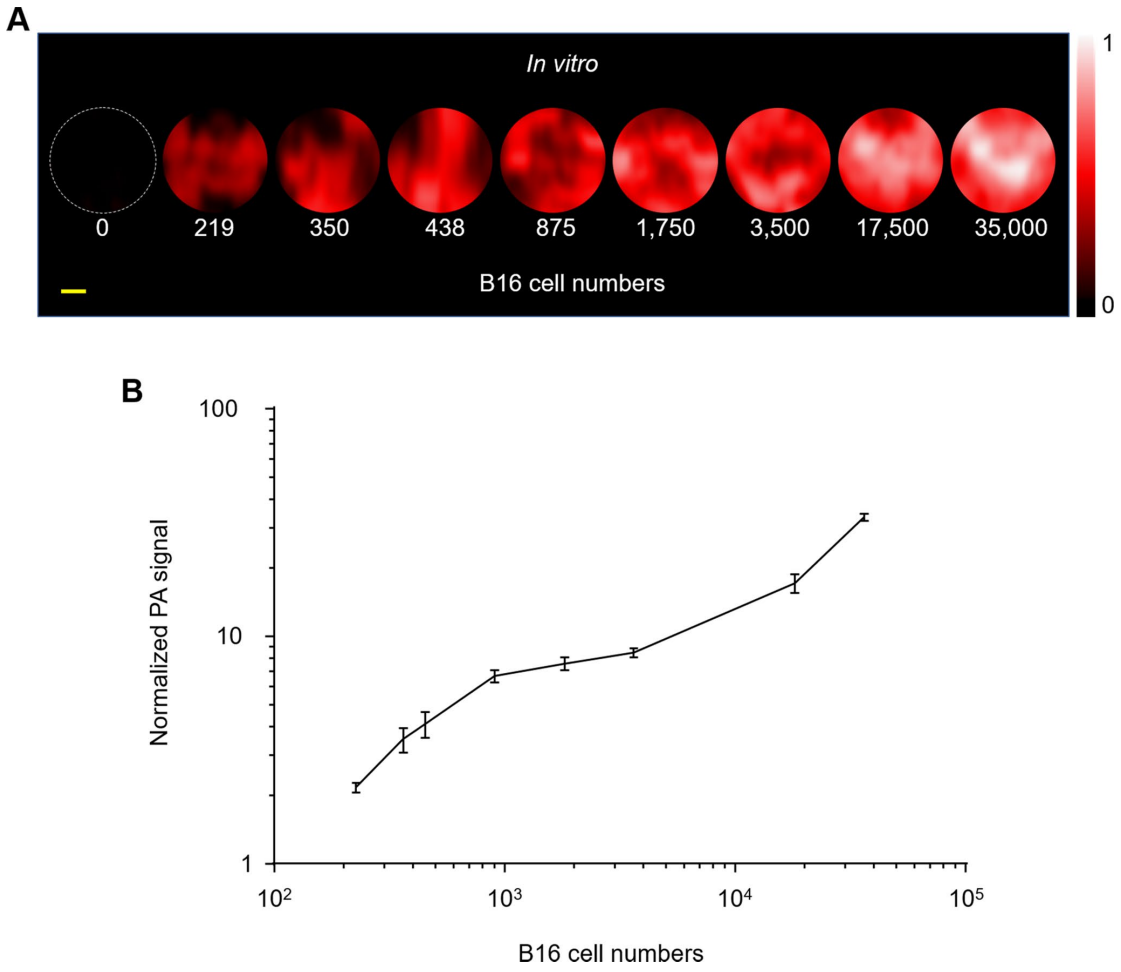

Supplemental Figure 2. Detection sensitivity of PAI in vitro. (A) Lowest density of live B16 melanoma cells in suspension that could be detected with PAI were ~219 cells per microliter PBS. Scale bar was 1 mm. (B) Graph shows relationship between cell density and PA signal in comparison with PBS control. PA = photoacoustic.

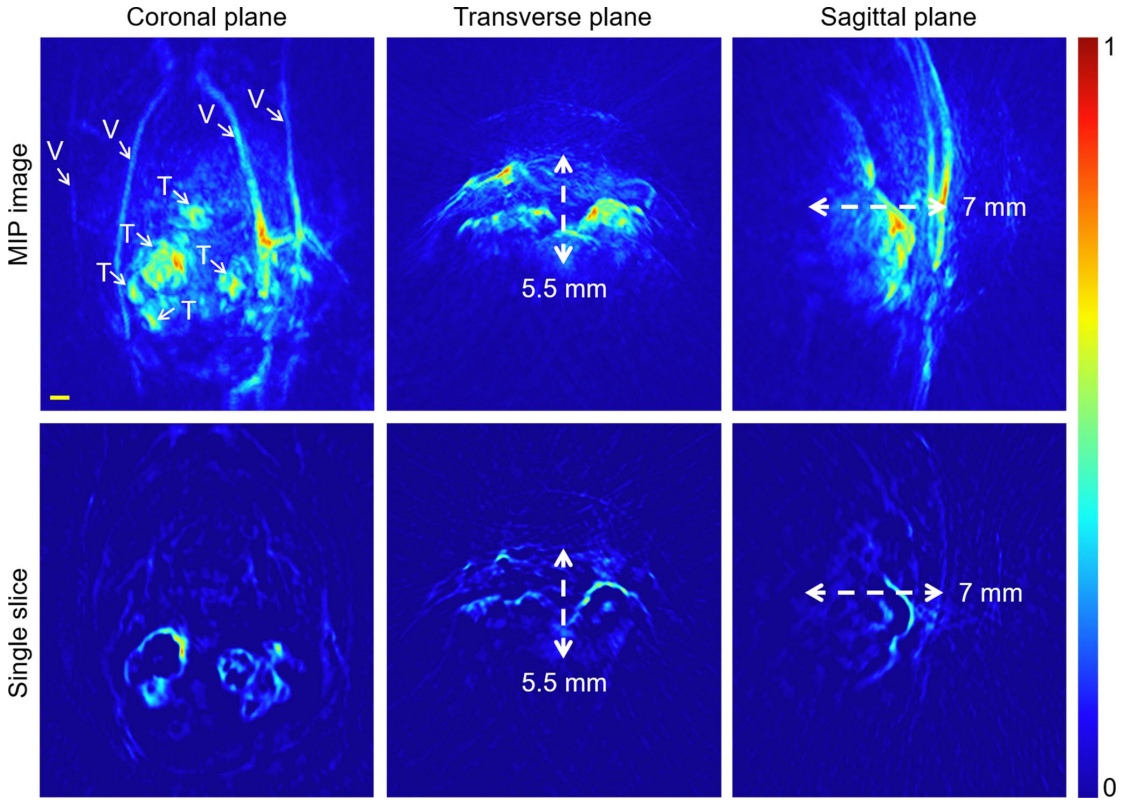

Supplemental Figure 3. Imaging depth characteristics of PAI in vivo. The coronal, transverse, and sagittal plane from a MIP image for mouse hepatic melanoma metastasis respectively were shown at 780 nm. The main vessels and tumors could be clearly detected. The coronal, transverse, and sagittal planes of a single slice were also shown respectively. A single slice for penetration depth of 7 mm was displayed in the sagittal plane. Scale bars in all images were 1 mm. V = vessels; T = tumor; MIP = maximum-intensity projection.

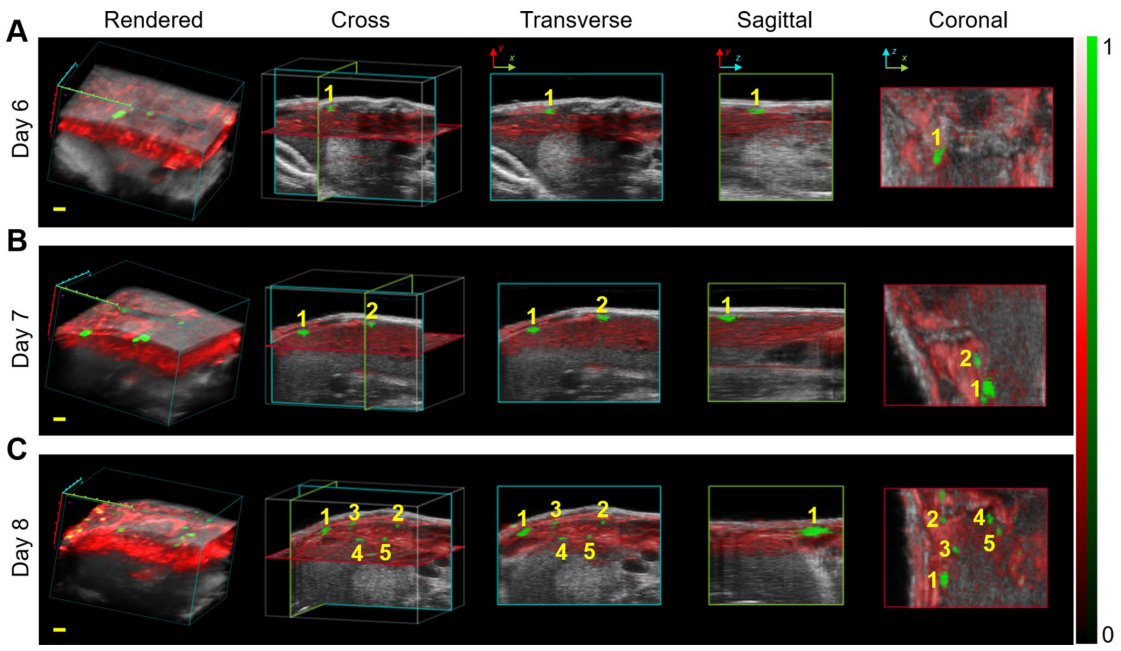

Supplemental Figure 4. Non-invasive in vivo PA and US imaging of melanoma liver metastasis mouse in Day 6, Day 7, and Day 8, respectively. 3D melanoma (green) and hemoglobin (red) distributions were estimated by spectral unmixing analyses from spectroscopic acquisitions at 680, 730, 924, and 950 nm, respectively. Render, cross, axial, sagittal and coronal images showed tumor distribution on (A) Day 6, (B) Day 7, and (C) Day 8, respectively. Scale bars in all images were 1 mm.

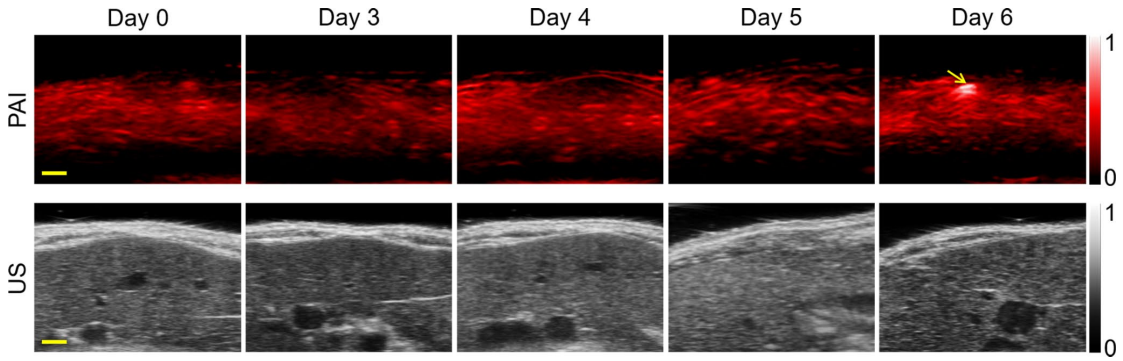

Supplemental Figure 5. Non-invasive in viv*o* PA and US imaging of melanoma liver metastasis mouse from Day 0 to Day 6. Scale bars in all images were 1 mm.

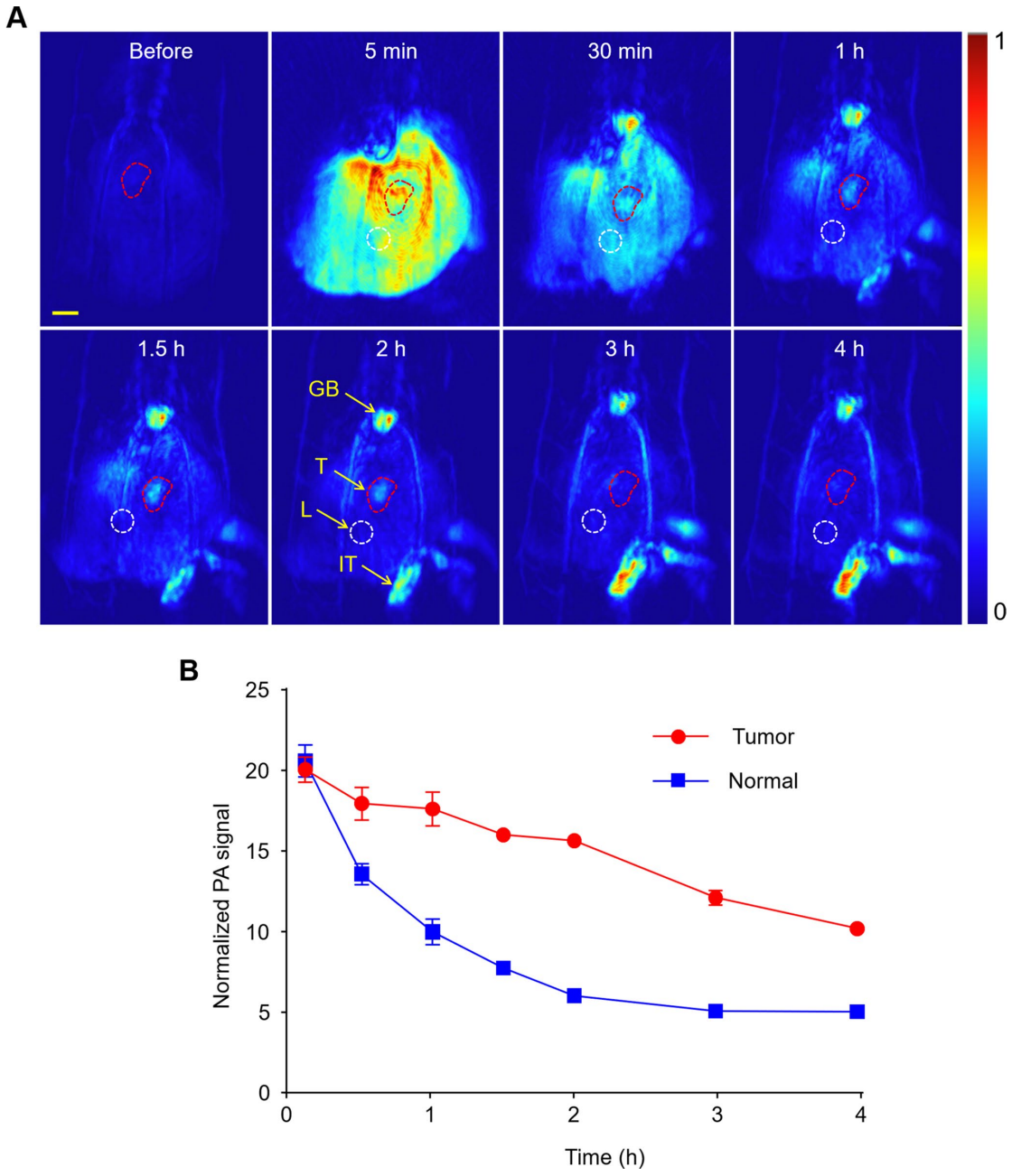

Supplemental Figure 6. Pharmacokinetic monitoring for primary liver cancer mice with ICG. (A) PAI of primary liver cancer mouse after ICG injection at different time points. ICG was cleared rapidly in liver within 1 hour, but slowly in tumor. (B) Time-signal curves of tumor and liver after ICG injection. Normalized photoacoustic signal ratio of tumor to liver reached the maximum after 2 hours. Scale bars in all images were 1 mm. GB = gall bladder; IT = intestinal tract; T = tumor; L = liver.

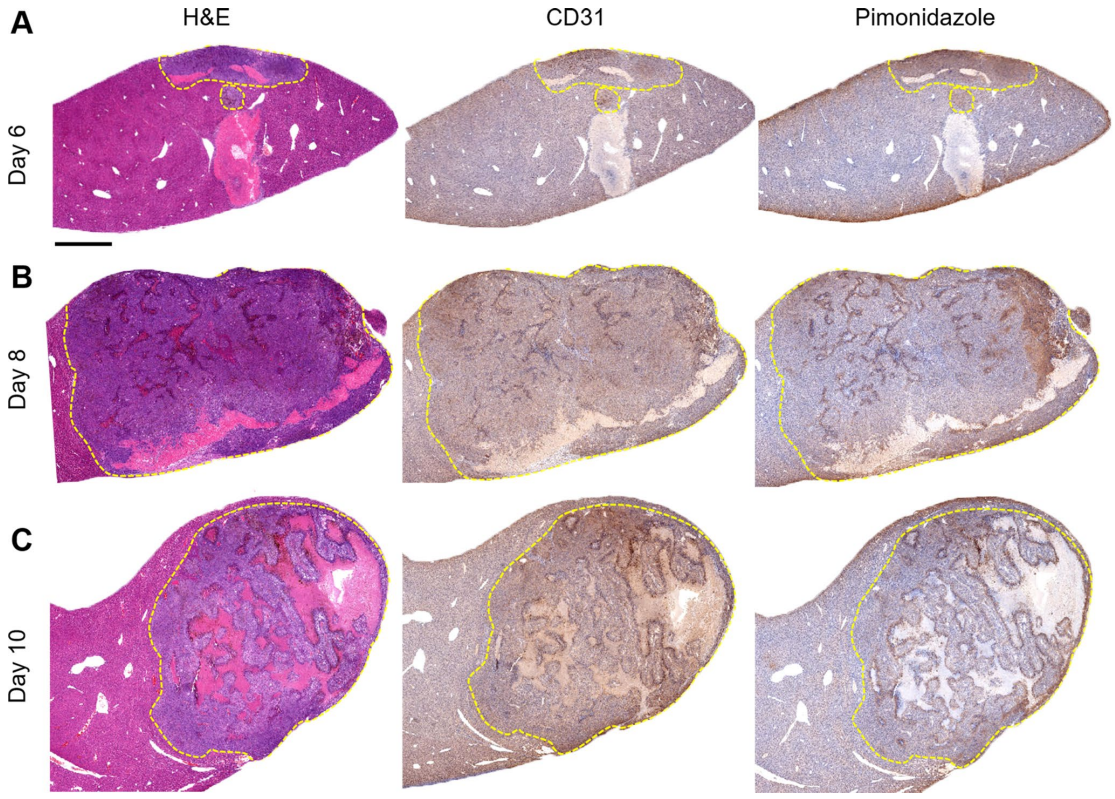

Supplemental Figure 7. H&E and IHC assessment of melanoma hepatic metastasis at different days. Tumor angiogenesis and hypoxic areas were stained with anti-CD31 antibody and anti-pimonidazole antibody respectively at (A) Day 6, (B) Day 8, and (C) Day 10. All ROI represents the tumor in liver. Scale bars in all images were 1 mm.

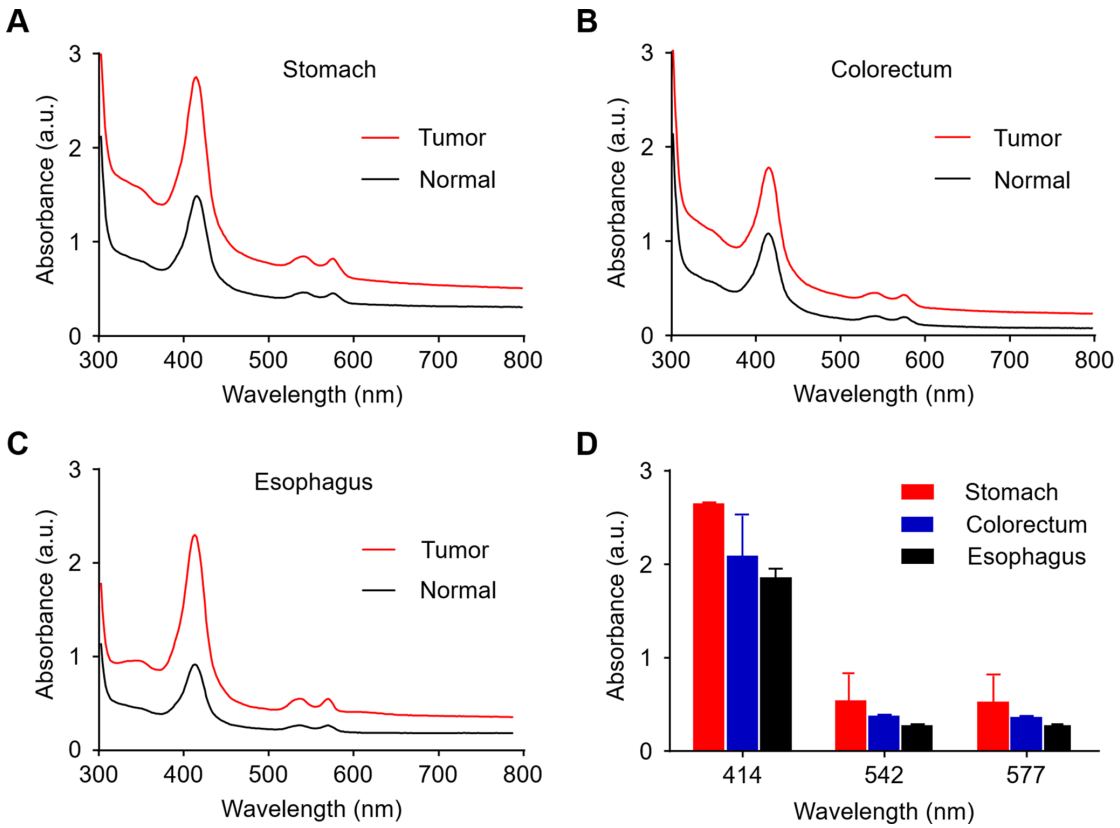

Supplemental Figure 8. The absorption of tissues at different wavelengths. (A) Stomach tissue. (B) Colorectum tissue. (C) Esophagus tissue. (D) Comparison of light absorption for three kinds of tissues at 414, 542, and 577 nm.

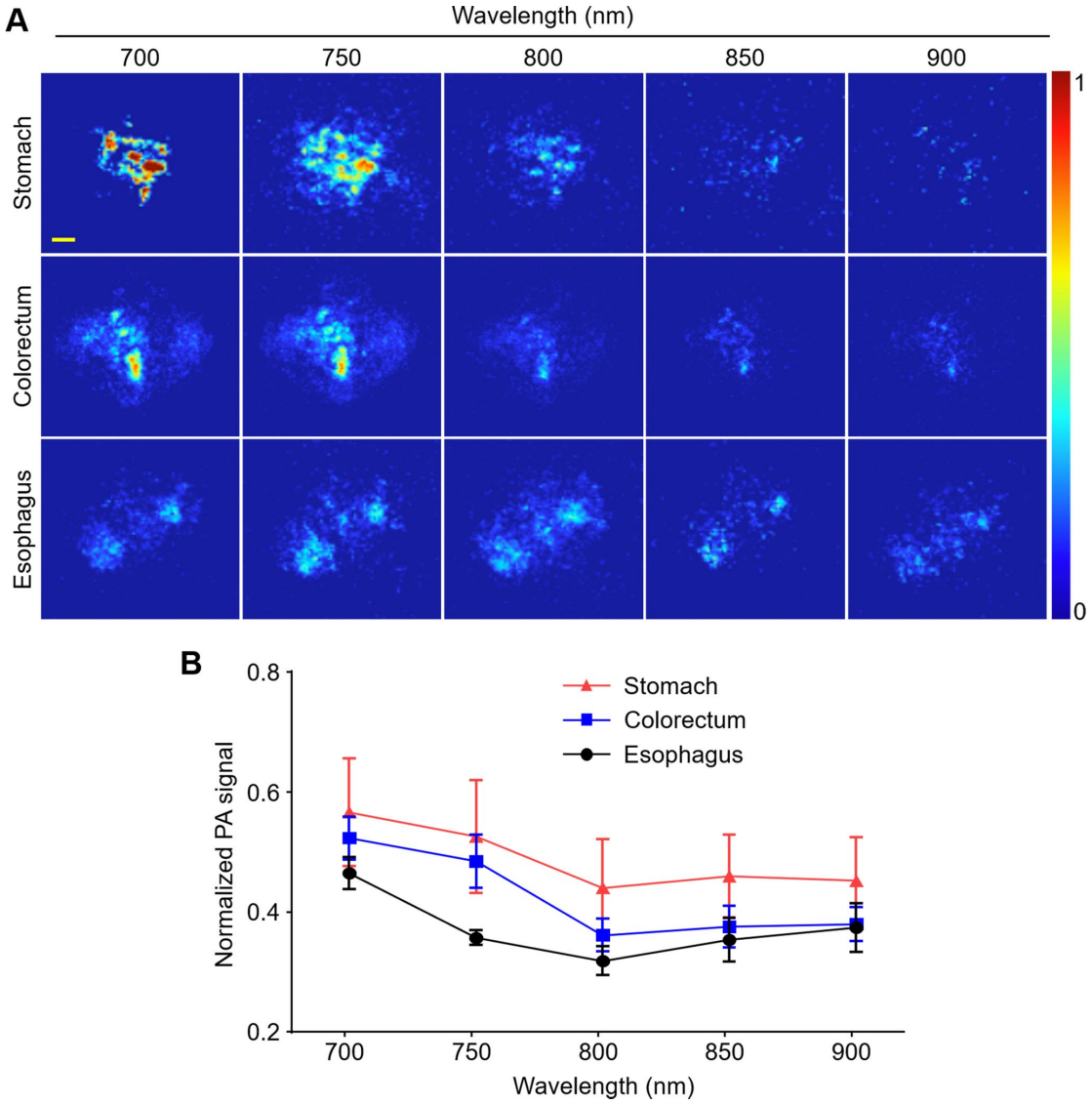

Supplemental Figure 9. PAI of gastrointestinal tumors at different wavelengths. (A) PA images of tumor tissue at 700, 750, 800, 850, and 900 nm. Scale bars in all images were 1 mm. (B) The PA signal intensity analysis.

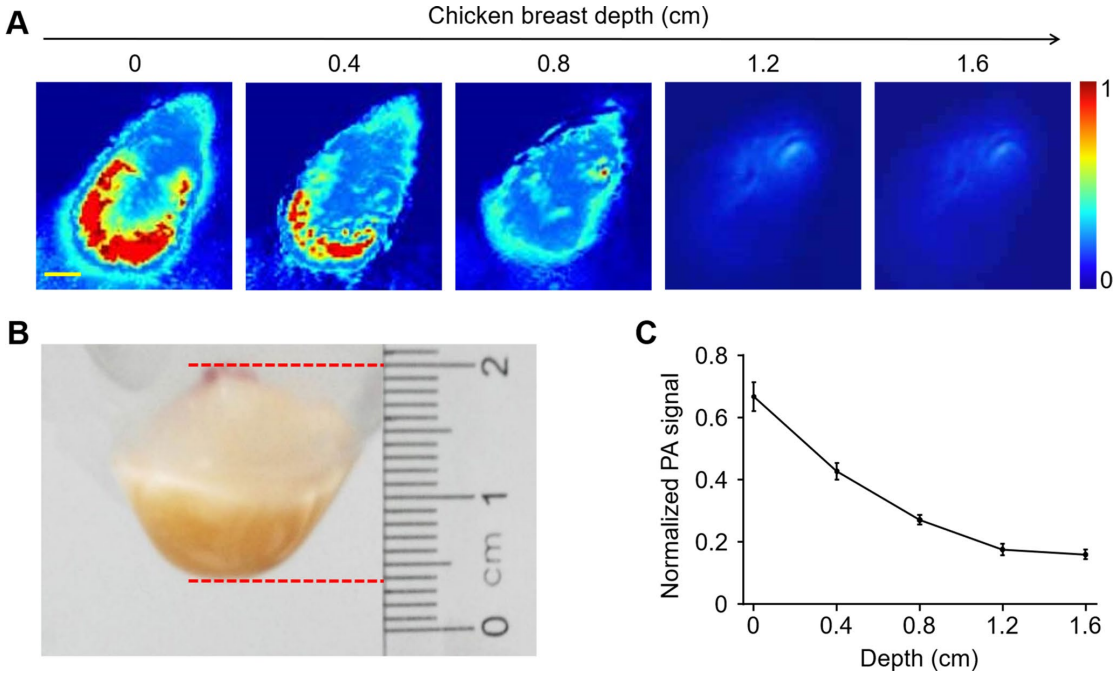

Supplemental Figure 10. Detection depth of PAI at phantom. (A) PA images of tumor tissue in chicken breast with different thicknesses (0.4, 0.8, 1.2, and 1.6 cm) at 750 nm. Scale bars in all images were 1 mm. (B) The photo of tumor tissue embedded in 1.6 cm chicken breast. (C) Corresponding normalized PA signal intensities versus imaging depth.

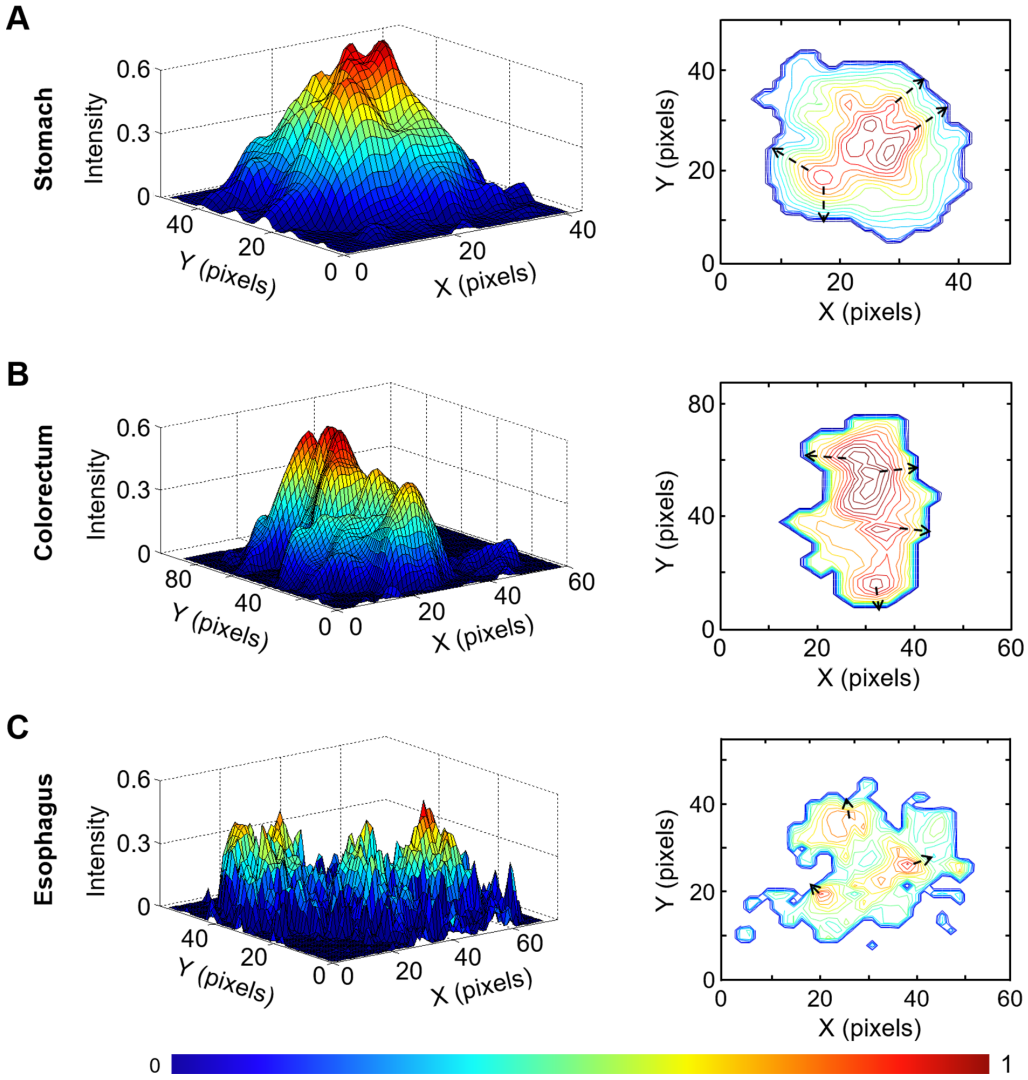

Supplemental Figure 11. Contour characterization for PA image of tumor tissue. The three-dimensional model and contours of PA image for (A) gastric, (B) colorectal and (C) esophageal tumor respectively.

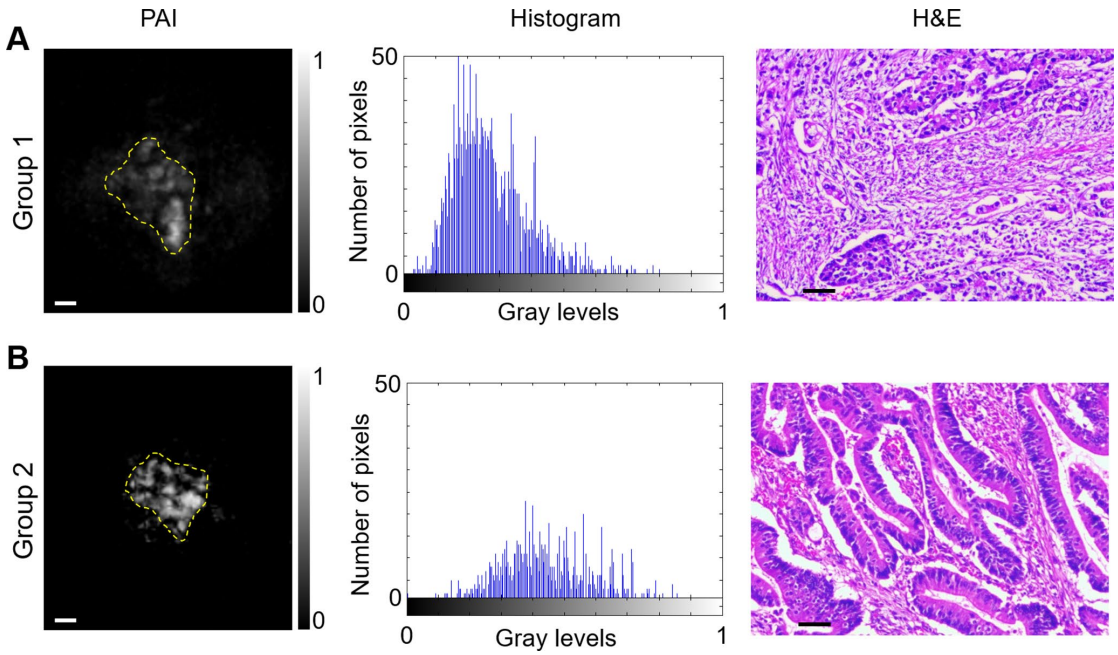

Supplemental Figure 12. Histogram and pathological analysis of PA images between group 1 (poorly differentiated tumor) and group 2 (moderately differentiated tumor). (A) PA grayscale image, histogram of tumor area, and histological images were shown for poorly differentiated tumors respectively. (B) PA grayscale image, histogram of tumor area, and histological images were shown for moderately differentiated tumors respectively. Scale bars of PA images were 1 mm. Scale bars of histological images were 50 μm. PA = photoacoustic.

	Group 1 (n=4)	Group 2 (n=10)	*P*-value	AUC
Kurtosis	5.92±1.02	3.78±1.20	<0.001***	0.91
Skewness	1.77±0.21	1.20±0.52	0.004**	0.88
Mean	0.38±0.14	0.25±0.12	0.041*	0.77
Maximum	0.72±0.14	0.52±0.19	0.008**	0.85
Minimum	0.05±0.08	0.01±0.01	0.44	0.60

	Cut-off value	Sensitivity (%)	Specificity (%)	PPV (%)	NPV (%)
Kurtosis	5.40	70	90	87.5	75
Skewness	1.46	90	70	75	87.5
Mean	0.31	70	90	87.5	75
Maximum	0.62	70	90	87.5	75

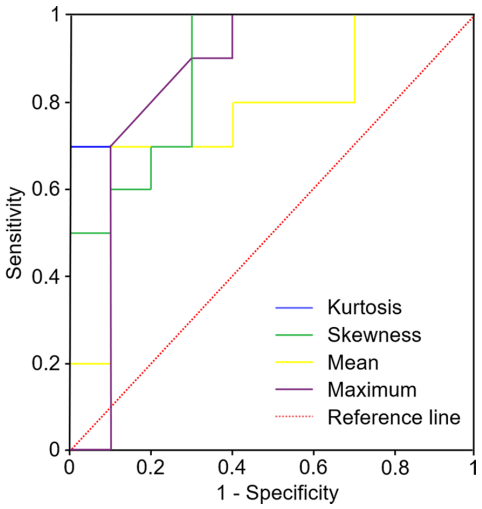

Supplemental Figure 13. ROC curve of histogram parameters (kurtosis, skewness, mean, maximum, and minimum) in differentiating group 1 and group 2. Data are presented as the mean ± standard deviation. $P < 0.05$*, $P < 0.01$**, $P < 0.001$***. ROC = receiver operating characteristic; AUC = area under the receiver operating characteristics curve; PPV = positive predictive value; NPV = negative predictive value.

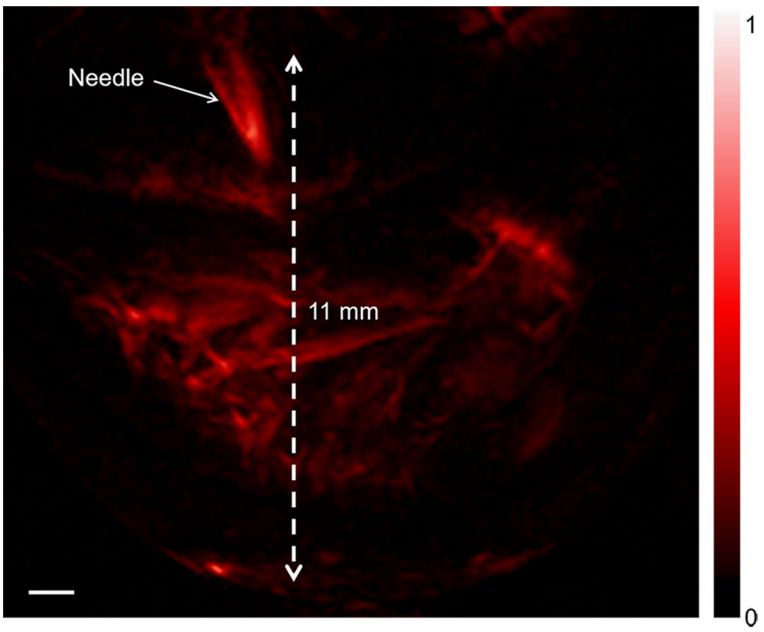

Supplemental Figure 14. Ex vivo liver lobes were stacked by inserting a needle into the upper lobe and placed in the tray imaged at 780 nm. The maximum imaging depth reached 11 mm. Scale bar was 1 mm.

Supplemental Video 1. Portable PAI of melanoma hepatic tumor at 7 days. 3D melanoma (green) and hemoglobin (red) distributions were estimated by spectral unmixing analyses from spectroscopic acquisitions at 680, 730, 924, and 950 nm, respectively.

Supplemental Video 2. Portable PAI of melanoma hepatic tumor at 10 days. 3D melanoma (green) and hemoglobin (red) distributions were estimated by spectral unmixing analyses from spectroscopic acquisitions at 680, 730, 924, and 950 nm, respectively.

Supplemental Video 3. Portable PAI of melanoma hepatic tumor at 14 days. 3D melanoma (green) and hemoglobin (red) distributions were estimated by spectral unmixing analyses from spectroscopic acquisitions at 680, 730, 924, and 950 nm, respectively.

Supplemental Video 4. High-resolution PAI of melanoma hepatic metastasis at 7 days.

Supplemental Video 5. High-resolution PAI of melanoma hepatic metastasis at 14 days.

Supplemental Video 6. Needle insertion and surgery with photoacoustic image-guided for melanoma hepatic metastasis.